PHYSICAL REVIEW D VOLUME 22, NUMBER 11 1 DECEMBER 1980

Proton polarization in *pp* elastic and inclusive processes at beam momenta from 20 to 400 GeV/*c*

M. Corcoran,* S. C. Ems,[†] S. W. Gray, R. M. Lepore, H. A. Neal, H. A. Ogren, R. O. Polvado,[‡] D. R. Rust,
J. R. Sauer,[§] and G. A. Walters[‖]
Department of Physics, Indiana University, Bloomington, Indiana 47405

(Received 30 January 1980)

The polarization of the recoil proton has been measured in both high-energy elastic and inclusive proton-proton scattering at the internal-target area of Fermi National Accelerator Laboratory. The polarization in elastic scattering was measured at a number of center-of-mass energies up to $\sqrt{s} = 19.7$ GeV. Indications of negative polarization were seen at the higher center-of-mass energies for t values of -0.6, -0.8, and -1.0 $(\mathrm{GeV}/c)^2$. In the inclusive process $p + p \rightarrow p_{\uparrow} + X$ the polarization was found to be independent of beam energy from 100 to 400 GeV for x_F values of -0.7, -0.8, -0.9. The polarization at $P_T = 1.0$ GeV/c, $x_F = -0.7$ and $x_F = -0.8$ was less than 2.5%. This is significantly lower than the corresponding measurements reported for Λ^0 inclusive polarization.

I. INTRODUCITON

This paper describes the results of two experiments designed to investigate spin effects in high-energy proton-proton collisions. Using the internal-target facility at Fermilab, we studied the polarization in both elastic and inelastic reactions as a function of incident beam energy and the momentum transfer to the outgoing proton. In both experiments to be described in this article we measured the polarization of a relatively slow recoil proton by rescattering it in a carbon block of known analyzing power and observing the left-right asymmetry. This conventional technique was refined in two important ways: (1) we used a hardware event processor to reject events where the rescattering of the protons in the carbon had little or no analyzing power; (2) we reduced systematic errors in the asymmetry measurements by taking data with the polarimeter in two orientations in which left and right were interchanged by rotating by 180° about the axis of the incoming beam.

In the elastic scattering experiment we traced the energy dependence of the polarization out to 200 GeV/c beam momentum from the previously measured lower energies of ANL,[1] CERN,[2,3] and Serpukhov.[4] In the inclusive experiment we were able to span the beam momentum range 100 to 400 GeV/c. We concentrated on the transverse momentum range $0.5 \rightarrow 1.5$ GeV/c, since indications of Λ^0 polarization[5] at $P_T = 1.0$ GeV/c emphasized the importance of a measurement of a related process such as $pp \rightarrow p_{\uparrow} + X$ in the same kinematic region. The kinematic regions are shown in Fig. 1.

These experimental results, along with the recent high-P_T scattering experiment at ANL,[6] and the inclusive Λ^0 polarizations found at Fermilab[5] and CERN ISR[7] indicate that spin-dependent effects still persist at high energies. In fact it appears that spin-dependent forces may dominate in certain high-energy processes.

Some of the results of these experiments have appeared in previous publications.[8,9] In this article we will present the details of the experimental setup, a discussion of the analysis, comparisons with several theoretical models, and tables of all measured polarizations.

The article is divided into five sections. In Sec. II we describe the experimental setup for both the elastic and inclusive measurement.

Section III contains the analysis procedure. Track reconstruction and determination of asymmetry were very similar for both elastic and inclusive experiments; however, the background and consistency checks are treated separately.

In Sec. IV we include a detailed discussion of

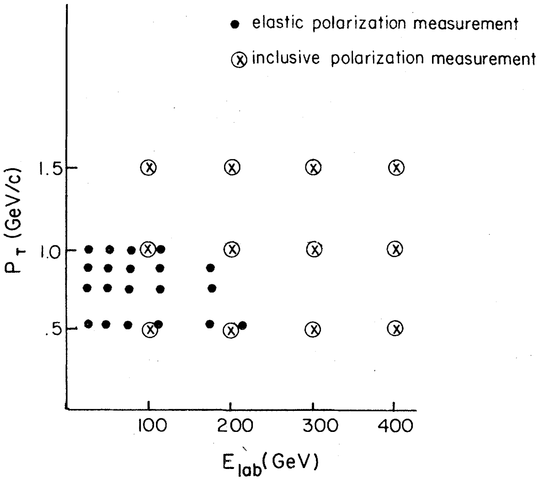

FIG. 1. Kinematic points for elastic and inclusive experiments. Data for inclusive experiments were taken at $x_F = -0.9$, -0.8, -0.7 at each indicated point.

the data. Final tables of polarizations and kinematics are presented.

Section V contains the interpretations of results. The polarization in elastic scattering is compared to other experiments and to several theoretical models. The inclusive polarizations are used to estimate the relative sizes of spin-flip and nonflip scattering amplitudes, and a comparison is made to both a triple-Regge model and a gluon bremsstrahlung model for inclusive polarization.

In Sec. VI we present a brief summary of the principal results of these experiments.

II. DESCRIPTION OF EXPERIMENTAL SETUP

A. The target and the beam

The experiment was performed at the CO internal-target area at Fermilab. Targets of two types were used. One was a hydrogen gas jet target operating with the gas at ambient temperature[10]; the other was a rotating carbon target.

The general features of the jet target are shown in Fig. 2. Hydrogen gas under pressures between about 6 and 20 atmospheres was forced through a 75-μm de Laval nozzle. The nozzle produced a jet of hydrogen gas about 5 mm wide with a small divergence. Because of the small divergence of the jet, the nozzle was placed above the vertical aperture of the beam and the jet was directed through the conical interceptor below the vertical aperture. The result was that most of the hydrogen (~85%) did not enter the beam pipe and the jet had a high density and a well-defined profile when it crossed the beam. Below the interceptor was a large buffer volume which reduced the rise in pressure and kept the pressure within the operating range of the vacuum pump. Large pumps were also employed in the target box to pump the fraction of gas which missed the interceptor.

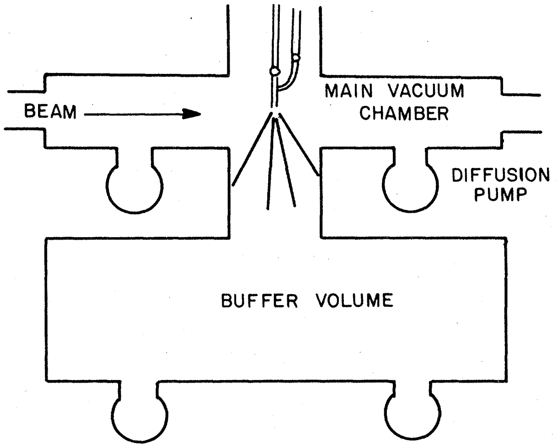

FIG. 2. Elevation schematic of warm gas jet target.

This apparatus gave an effective target thickness as large as 10^{-7} g/cm^2 during this experiment. The normal mode of operation was to pulse the jet on for 100 msec at each of four or five times the accelerating cycle. The limitation on the amount of hydrogen arose from the effect on the beam of accumulated gas in the beam pipe during the accelerating cycle. The extraction efficiency is sensitive to the quality of the beam and the external experimental areas get reduced beam if the gas pressure is high.

The rotating carbon target was assembled into the same target box as the jet. Either one could be used with only a small delay required to change from one to the other. The carbon was in the form of carbon fibers extending from the surface of a wheel which rotated at 3600 rpm. The rotating target was set at a fixed position so that the beam intercepted it throughout the accelerating cycle.

The incident beam was the primary accelerated proton beam. It was injected at 8 GeV/c and by the time it was accelerated to 20 GeV/c it was well focused and the orbit was stable. The maximum energy was normally 400 GeV and any energy between 20 and 400 GeV was available at some time in the accelerating cycle.

The intensity of the beam was as high as 2×10^{13} protons and the number of traversals was 4.8 $\times10^4$/sec. This resulted in an effective intensity of 1×10^{18} protons/sec during the cycle. The most probable intensity was about half this number. The duty cycle is the product of the frequency of accelerating cycles (0.10 to 0.16 Hz) times the data collection time in each cycle. Usually the data collection time was 0.1 sec at each of five energies. The duty cycle was therefore typically 0.06. These numbers give a luminosity of typically 1.5×10^{34}/cm^2 pulse or 2×10^{33}/cm^2 sec, but it ranged as high as three times this number depending on the operation of the accelerator, the type of target, and the rate of collecting data. These luminosities were comparable with what can be obtained with liquid targets in an external beam line.

B. Spectrometer

Particles produced in the target were focused by a superconducting quadrupole doublet (Q1-Q2 in Fig. 3). The quadrupole doublet increased the angular acceptance to ±2.88 degrees in the vertical plane and ±0.57 degrees in the horizontal plane, a factor of 40 increase in the solid angle acceptance over that without quadrupoles. The quadrupoles had a parallel to point focus at the first spectrometer proportional chambers (SCS1-3); therefore, a position measurement in the first

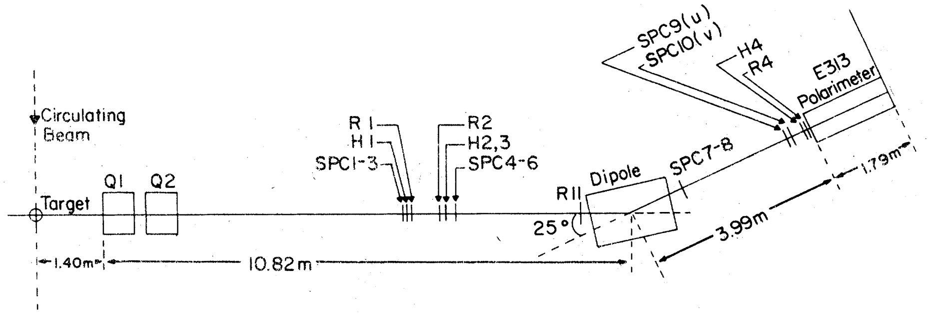

FIG. 3. Plan view of internal-target spectrometer.

chamber corresponded to a measurement of the production angle at the target.

Multiple scattering was kept to a minimum by enclosing all major paths in the spectrometer in a helium atmosphere. The path of the proton from the target to the first quadrupole was through vacuum.

The momentum analysis was provided by a superconducting dipole (Fig. 3). A map of the dipole field was made using a Hall probe during the construction of the spectrometer. The field inside the magnet was found to be uniform to within ±3%, but large fringe fields were found outside the magnet proper. This necessitated the use of second- and third-order matrix elements in the momentum analysis. Initially the spectrometer had a bend angle of 25 degrees, but midway through the inclusive experiment the bend angle was changed to 17 degrees to permit the analysis of scattered particles of higher momentum.

The location of the spectrometer chambers (SPC1-11) and hodoscopes (*H*1-4) are shown schematically in Fig. 3. All chambers had a wire spacing of 1.3 millimeters and were filled with the standard "magic gas" mixture of 20% isobutane, about 0.4% freon, and the balance being argon. This gas mixture was bubbled through a methylal bath at 5°C. The first spectrometer-chamber set (SPC1-3) was used to determine the production angle at the target. The seven chambers before the dipole (SPC1-7) were used to determine the position of a particle between SPC5 and SPC6 and the entry angle to the dipole, while the four chambers behind the dipole (SPC8-11) were used to determine the particle position between SPC10 and SPC11 and the particle exit angle from the dipole. This information was used to calculate the momentum of the particle. The hodoscopes were used to resolve ambiguities in the track reconstruction at a bend angle of 25 degrees and were not used in the momentum analysis at a bend angle of 17 degrees.

Four trigger counters (*S*1-4) were available for use in defining a good spectrometer event. The positions of the counters may be found in Fig. 3. A second use of *S*1 was as part of a time of flight system which was used for particle identification. In the inclusive experiment a 1.27 cm thick scintillator, which was twice the thickness of the scintillator used in the other trigger counters, was used in *S*1 for increased time resolution and greater pulse height. This pulse was fed to a constant fraction discriminator whose output was then used as the start pulse of a time-to-digital converter (TDC). At low momenta in the elastic scattering experiment a 0.32-cm-thick counter was used in order to reduce multiple scattering.

C. Polarimeter

The Indiana polarimeter (Fig. 4) was constructed to utilize the known spin-analyzing power of carbon. To achieve this, the polarimeter was designed to measure the left-right asymmetry in the distribution of particles scattered by a 5-cm-thick carbon block, whose analyzing power had been measured using the polarized proton beam of the Argonne National Laboratory Zero Gradient Synchrotron (ZGS).[11] Chamber telescopes before and

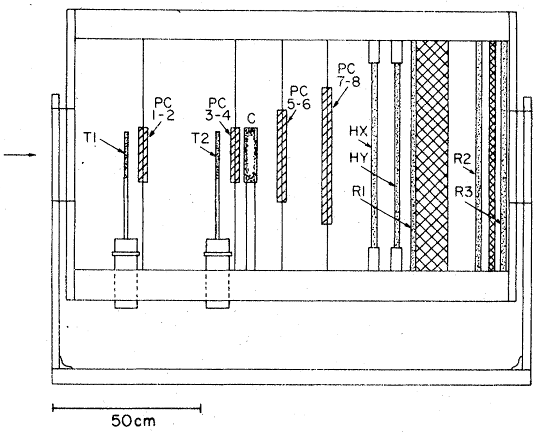

FIG. 4. Indiana carbon polarimeter.

after the carbon block (PC1–8) were used to define particle trajectories. A set of X and Y hodoscopes (HX and HY in Fig. 4) were available to resolve ambiguities in track reconstruction for the chamber telescope behind the carbon block. A set of range counters ($R1$–3 in Fig. 4) were part of the polarimeter but were not needed in this experiment.

The polarimeter chamber telescopes were composed of four multi-wire proportional chambers with a wire spacing of 2 mm. The standard magic gas described earlier was also used in these chambers. One of the unique features of this experiment was the ability of the polarimeter to rotate 180 degrees about the incoming beam direction. By averaging the data at the two orientations instrumental asymmetries could be reduced or eliminated.

Two trigger counters ($T1$- and $T2$ in Fig. 4) were utilized to determine an event in the polarimeter. $T2$ was also used in the time-of-flight measurement. Like $S1$, $T2$ was made of 1.27-cm-thick scintillator for the inclusive experiment. The output of $T2$ was used as the input of a constant fraction discriminator, whose output was used as a stop pulse for a TDC. For the elastic experiment both $T1$ and $T2$ were 0.63 cm thick.

D. Fast logic for experiment

The polarimeter fast logic is shown schematically in Fig. 5. TR was defined as the coincidence between scintillators $S1$ and $S2$. TP was defined as a coincidence between $T1$ and $T2$. Throughout the experiment an EVENT was defined to be a coincidence between TP and TR. Since for different momenta, the transit time in the spectrometer varied, an adjustable delay was used in the cable between TR and EVENT to maintain the coincidence timing between TR and TP.

The strobes for the spectrometer and polarimeter chambers were produced by the outputs of TR and TP, respectively. The chamber information was then stored in a shift register awaiting a decision on whether an acceptable event had occurred.

E. Polarimeter computer

The polarimeter computer was a hardware preprocessor designed to test each event and decide if it was to be recorded. Since the analyzing power of the carbon block was measured between 6 and 22 degrees,[11] a useful event was one which fell in this range. Three tests were made in both the X and Y planes in the polarimeter to make this decision; (1) an "upstream" test, (2) a "straight-through" test, and (3) a "scatter" test.

The upstream test was made in the front chambers (PC1–4) to determine that there was at least one "hit" wire in all four chambers and that a track existed which was reasonably parallel to the beam direction. The accepted angle of deviation from parallel could be selected to be in the range ±13 mrad, ±26 mrad, or ±39 mrad. For a successful upstream test a track must pass the above tests in both the X and Y planes. Upon a successful result of the test, the tracks found in the upstream test were projected to the back polarimeter chambers to determine which wires would have been hit if the particle did not interact in the carbon block. These predicted hits in the back cham-

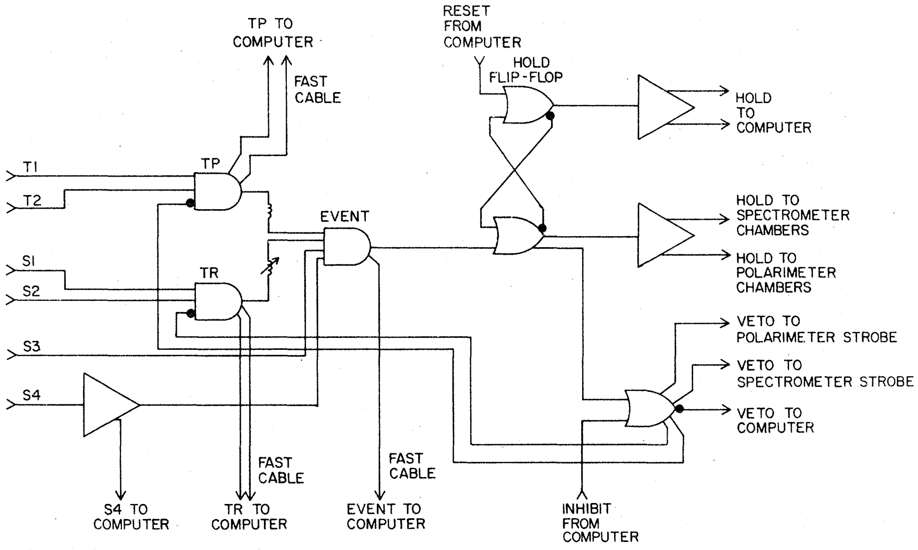

FIG. 5. Principal fast-logic layout.

bers were then used in the straight-through test.

The straight-through test was made to test for events which did not scatter at large enough angles. The predicted hit positions in the back chambers were associated with a particular bit in a shift register. The polarimeter computer would then look for a straight-through track by shifting the shift registers to determine if a hit had occurred within a certain number of shifts of the predicted wire hit. The number of shifts used to determine if a track was a straight-through track was set so that scatters of less than 4 degrees would be rejected. The angle of 4 degrees was selected so that most straight-through events would be rejected but the chance of the polarimeter computer interfering with the data in the desired angular region would be small. If a straight-through track was sensed in both planes the event was rejected unless the alignment check was being made.

The scatter test was made by continuing the shifting in the shift registers and looking for a track at large angles. The tolerances were set to accept any track which scattered between 4 and 30 degrees. An event passed the scatter test if a track which satisfied the scatter requirement was found in either plane.

Any or all of the above tests could be included in the definition of a good polarimeter computer event. The tests were always used in sequence because the straight-through test was useless without the upstream test and the scatter test did not make sense without the straight-through test. All tests could be used in two different modes. The polarimeter could tag each event as to which tests it passed and always send a polarimeter event signal, or it could send a reject signal if an event failed any one or all of the tests and a good signal if an event passed the tests. In the latter mode the polarimeter computer would also take a data buffer of tagged events every 16 beam ramps, to be used as a check on how the system was running. When all of the tests were used, a decision typically could be reached in 2 μsec. A polarimeter-event signal was used to activate the data-acquisition system. A polarimeter-reject signal was used to generate a RESET signal which was used to reset the fast logic and clear all units in the CAMAC crate so that a new event could be accepted.

III. ANALYSIS OF DATA

A. Momentum calculation

The spectrometer hodoscopes were used to filter out spuriously hit wires in the spectrometer proportional chambers. If more than two hits occurred in a chamber, then the filter would pass only those hits for which a hodoscope element had fired at approximately the same position. Once the filtering was complete, only those events which had at most one hit wire per chamber were momentum analyzed. The momentum was calculated by a standard algorithm with a six-component vector q, where

$$q_1 = x\,,$$

$$q_2 = dx/dz\,,$$

$$q_3 = y\,,$$

$$q_4 = dy/dz\,,$$

$$q_5 = \text{bunching parameter}\,,$$

$$q_6 = (\Delta p)/p_{\text{zero}}\,,$$

which satisfies the equation

$$X = \sum_i A_i q_i + \sum_{ij} B_{ij} q_i q_j\,.$$

In the above relations, z is the coordinate along the beam axis, x and y are the horizontal and vertical coordinates of a particle track at a particular value of z, p_{zero} is the momentum of a particle passing through the center of the dipole, $\Delta p = p - p_{\text{zero}}$, where p is the momentum of the particle, and X is the (x, y) coordinate of the particle. The bunching parameter described the structure of the beam, but was not important in this experiment as we average over 6000 beam transversals per jet. A Monte Carlo program was used to generate virtual particles which were tracked through the dipole using standard beam transport equations. These events were then used to determine the coefficients (A and B) of the above equation. After the constants were determined, then q_6 could be calculated whenever q_1, q_2, q_3, q_4, and X were known. q could be defined downstream ($z = 1578.6$ cm) of the dipole and X upstream ($z = 855.85$ cm) of the dipole (backward-momentum calculation), or q could be defined upstream ($z = 855.85$ cm) of the dipole and X downstream ($z = 1578.6$ cm) of the dipole (forward-momentum calculation). These two values were averaged to obtain a final momentum value.

As described earlier, the quadrupoles have a point to parallel focus on the first spectrometer chambers (SPC1–3), thus the x and y position of the track directly determined the production angle to first order. In a similar manner to the momentum calculation, the momentum was incorporated as a correction to the calculation of the production angles at the target. After the momentum and production angles of a particle were known, then the missing mass of the event was calculated.

B. Polarimeter track reconstruction

The chamber hit positions were decoded from the on-line measurement of the hit wires in each of the multiwire proportional chambers (MWPC). Since it was known that this discrete position determination could present problems in the asymmetry determination when angular cuts were applied, we randomized the track position about the individual wire coordinate. This reduced our sensitivity to small shifts in the angular cuts that we applied when calculating the left-right asymmetry. The effect of this procedure can be seen in Fig. 6. In this figure we show the incoming angular distribution in the X-Z plane (θ_x) using both discrete track coordinates and the randomized coordinates. All of the subsequent track analysis was done using these randomized coordinates.

The track reconstruction in the polarimeter was performed independently of the track reconstruction in the spectrometer. A coordinate system fixed in space and defined with Z along the beam direction, X horizontal, and Y vertical was used. The front face of the mounting plate of the first polarimeter chamber (PC1) corresponded to the $Z=0$ plane. Track reconstruction in the X-Z and Y-Z planes were made independently of each other.

In order to follow a particle through the carbon block, trajectories were formed upstream and downstream of the carbon block by taking the hits in the X chambers and letting these points define a line. A similar procedure was followed for the Y chambers. Using the chamber positions calculated earlier, all possible trajectories were formed upstream and downstream of the carbon block. These trajectories were projected along the z axis to the center of the carbon block. If the difference between the X and Y positions of the upstream and downstream trajectories at $Z=37.1$ cm (i.e., the center of the carbon block) fell within a certain tolerance, the two trajectories were assumed to be one track. The tolerance (D) was a function of the angle (A) between the upstream and downstream trajectories and the wire spacing of the chambers. For a wire spacing of 0.2 cm and a 5-cm carbon block,

$$D\,(\mathrm{cm}) = 0.635 + 2.54\tan(A)\,.$$

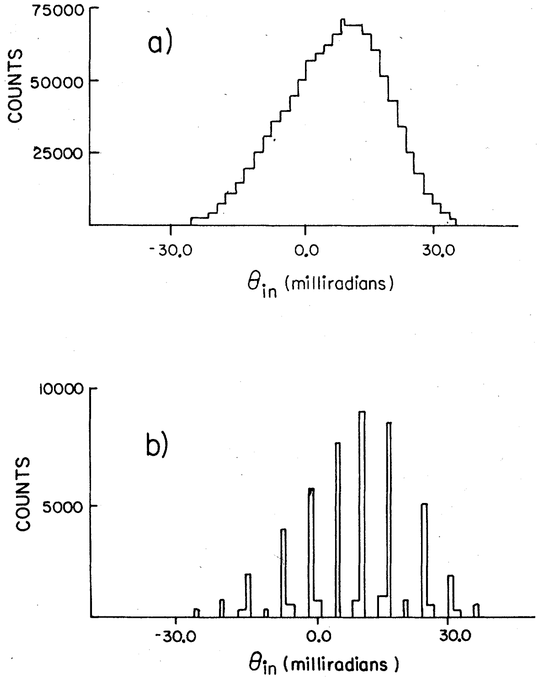

FIG. 6. Incoming angle θ_{in} for polarimeter track (a) with track-position randomization and (b) without randomization.

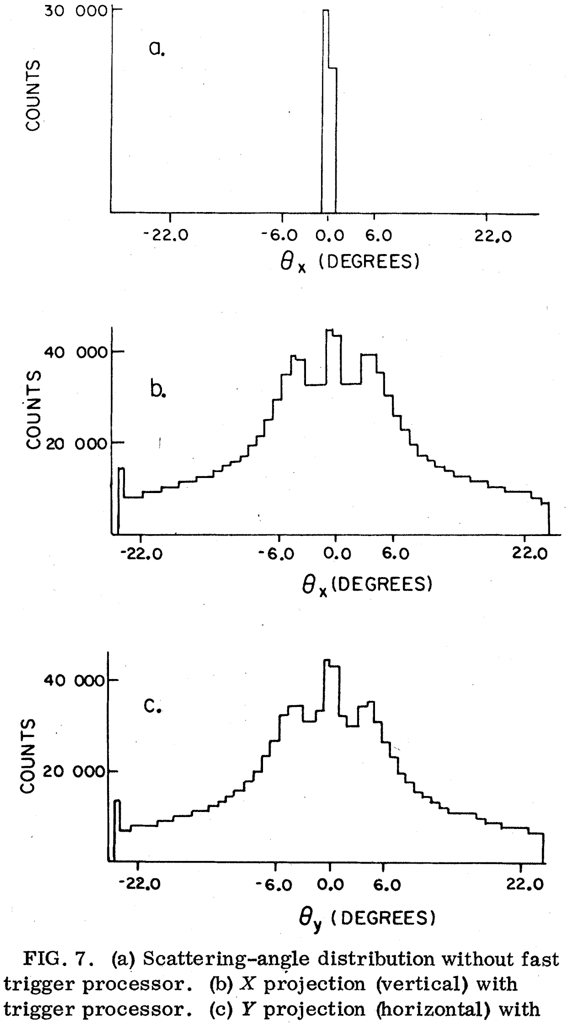

FIG. 7. (a) Scattering-angle distribution without fast trigger processor. (b) X projection (vertical) with trigger processor. (c) Y projection (horizontal) with trigger processor.

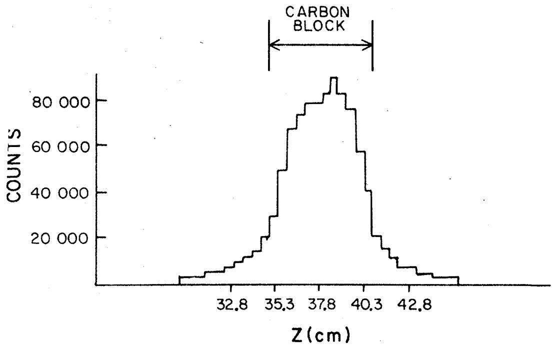

FIG. 8. Projected scattering point in carbon block (Z).

If two downstream trajectories were found to link to the same upstream trajectory, the track was assumed to be a V and the downstream trajectory making the smaller angle (A) with the upstream trajectory was used in the asymmetry calculations. If more than two downstream trajectories linked to the same upstream trajectory or two or more upstream trajectories were found to link to any downstream trajectory, then the event was considered unreconstructable in the X-Z (Y-Z) plane. These conditions on multiple track events were consistent with those used in determining the analyzing power of the carbon block.

Once the reconstruction was complete in the X-Z (Y-Z) plane, the projected scattering angle θ_x (θ_y) and the intersection point (vertex) of the upstream and the downstream trajectories were calculated (see Figs. 7 and 8). If, for an event, reconstruction was possible in both the X-Z and Y-Z planes, then the polar scattering angle (θ) and the azimuthal angle (ϕ) were calculated. After a successful reconstruction was found in the X-Z (Y-Z) plane, the track was projected to the appropriate hodoscope and a tag was set if the corresponding hodoscope element had fired, but the hodoscopes were not used to define a good track.

C. Efficiencies

Since an inefficiency in one of the downstream chambers could produce an asymmetry, the efficiencies of the downstream polarimeter chambers and the polarimeter hodoscopes were calculated for each run. It was not necessary to calculate the efficiencies of the upstream chambers as they would have no effect on the asymmetry. This instrumental asymmetry would, in principle, be removable by averaging the data from the 0 and 180 degree orientations. An exception to this could occur if the chamber efficiencies at 0 degrees would differ from those at 180 degrees. Each downstream chamber was divided into a 12×12 array and each hodoscope element was divided into 12 sections, and then the efficiencies were calculated for each section.

Only those events in which only one hit occurred in each of the four upstream chambers and a single X and Y hodoscope element fired were used in the chamber efficiency calculation. A straight-line trajectory was formed from the center of the elements defined by X-Y hodoscope intersection to the intercept of the upstream trajectory at $Z=37.1$ cm (the center of the carbon block). The section of the rear chambers through which the trajectory passed was assumed to be hit. The efficiency was the ratio of the number of times a hit was found in the predicted section of the chamber to the number of projected hits. The chamber efficiencies were greater than 98% for all 144 sections, and more importantly, no variations were observed when the chambers were rotated.

D. Asymmetry and polarization

The asymmetry (ϵ) is defined by

$$\epsilon=(L-R)/(L+R)\,,$$

where L is the number of left scatters and R is the number of right scatters. The polarization (P) could then be calculated from

$$\epsilon=-PA\,,$$

where A is the analyzing power of carbon. The sign convention is explained in Appendix I. In a previous experiment,[11] the analyzing power of carbon was measured using the polarized proton beam at the ZGS. The analyzing power was calculated by measuring the asymmetry for typical beam polarizations of 70–80%. The polarization of the beam was periodically reversed in order that instrumental asymmetries could be reduced by averaging the runs of different polarization. Since in the ZGS experiment, the analyzing power was measured for $|\theta_x|$ between 6 and 22 degrees, the asymmetry in these experiments also was determined for $|\theta_x|$ between 6 and 22 degrees.

The chamber efficiencies were incorporated into the asymmetry calculation, by weighting each left or right scatter by the inverse of the combined chamber efficiencies. The corrected chamber asymmetry (ϵ') was then

$$\epsilon'=(L'-R')/(L'+R')$$

with

$$L'=\sum_i 1.0/W_i \quad R'=\sum_i 1.0/W_i\,,$$

where W_i is the weight for each left (right) scatter. As a check, the asymmetries were also calculated without the weighting procedure. We found that the unweighted asymmetries were always within one standard deviation of the weighted value.

E. Background

The largest category of background events in the experiment was of the type where a particle which did not pass through the dipole would enter the polarimeter. This could occur since the downstream chambers of the polarimeter could "see" the target region. This would cause an excess of right scatters and occurred either when a particle would stop in the carbon block and a downstream track was created by a background particle or when the track of a background particle could be incorporated with a real track to form a *V*.

The background was reduced by two separate techniques. For the inclusive measurements concrete shielding blocks were placed on a movable cart which was then attached to the spectrometer in such a manner as to block the line of sight between the polarimeter and the target region. Secondly, the background was reduced by restrictions in the analysis. A tight tolerance (*D*) was imposed [see Sec. III B] for a track link to occur between an upstream trajectory and a downstream trajectory. Also a requirement that an event have one and only one hit in SPC7 was imposed in order to demand that a particle had actually passed through the dipole.

F. Effect of the polarimeter computer

As stated in the previous chapter, the polarimeter computer was a critical feature of the experiment. If the polarimeter computer had not been used, the θ_x and θ_y distributions would be sharply peaked at 0 degrees. In Fig. 7, a histogram of θ_x is plotted for a run in which the polarimeter computer was not used. When compared to the plot of θ_x for data in which the polarimeter computer was used, the contrast is quite striking. The most dramatic way of demonstrating the effect of the polarimeter computer is to look at a scatter plot of θ_x versus θ_y. Such a scatter plot is shown in Fig. 9. The polarimeter computer makes a virtually square cut in the data. The edges of the square are well away from our asymmetry cut of 6 degrees.

G. Event selection and correction

In the final data sample strict criteria were used to determine which events would be used for the asymmetry calculation. In the inclusive experiment an event was required to have one and only one hit in SPC7 in order to require that a single particle had passed through the dipole. Upon entering the polarimeter, only those events in which all four upstream chambers had a single hit were used. This further reduced the chance of background events occurring. Also a successful track reconstruction was required in both the *X-Z* and *Y-Z* planes. In order to guarantee that the particle had scattered in the carbon block a cut was made on the vertex reconstruction. A cut on the time-of-flight spectrum was made to select protons (see Fig. 10). In the elastic scattering experiment the missing mass distribution was used to select a clean sample of elastic events. The data consisted of events taken for energy ranges centered at beam momenta of 22, 45, 75, 110, and 175 GeV/*c*. Figures 11(a)-(c) show some typical raw (missing mass)^2 − (proton mass)^2 distributions. For the lowest beam energy, essentially all of the events were elastic. As the beam energy increased, the number of inelastics increased. At high energies, and especially for the high $|t|$ values, there was a considerable inelastic contamination. The elastic events were determined by fitting the missing mass distributions with an empirically determined background shape and a symmetric elastic peak. The contamination was less than 10% in all cases for $t \leq -0.6$ (GeV/*c*)^2. For $t \geq -0.8$ (GeV/*c*)^2 the contamination was 17-18% for the three highest energies. The resulting corrections including those for any background asymmetries changed the observed asymmetry of the elastic peak by less than one-fourth of a standard deviation for all points except $t = -1.0$ (GeV/*c*)^2 and $E_{\rm lab} = 110$ GeV. For that point, the result was changed by a little less than one-half standard deviation. The estimated error was increased by 50% to account for this effect.

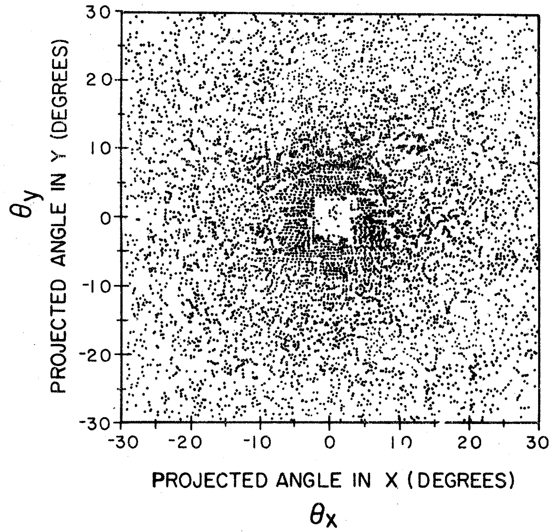

FIG. 9. *X* and *Y* projections of scattering distribution in carbon block. Central area shows the effect of the fast trigger processor.

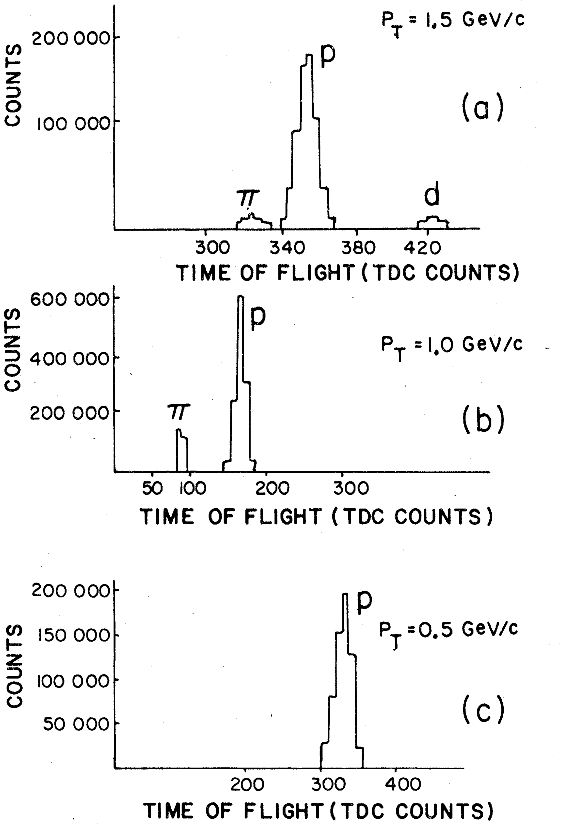

FIG. 10. (a) Time-of-flight spectra, $P_T = 1.5$ GeV/C. (b) Time-of-flight spectra, $P_T = 1.0$ GeV/c. (c) Time-of-flight spectra, $P_T = 0.5$ GeV/c.

H. Consistency tests

Several independent tests of the experimental apparatus were available for use in determining the reliability of the system. These include the results of previous experiments, the asymmetry of the pion data, the asymmetry in the Y-Z plane, the consistency of the data between running periods, and the agreement between the two orientations of the polarimeter. The polarization of the elastic proton for a beam momentum of 22 GeV/c agrees well with other experiments.[6]

Both pions and protons could be included in our data sample. Changing only the time-of-flight cut and repeating the analysis, the pion asymmetry could be determined. Since the pion is a spin-zero particle, the asymmetry must be zero. For those data points which contained pions, we found a zero asymmetry within statistical errors. In the proton data, the Y-Z (vertical) asymmetry was also calculated using the θ_y distribution. Polarization in this direction is forbidden by parity conservation. The Y-Z asymmetry was found to be consistent with zero. The magnitude of the asymmetry was less than 0.3% in all cases.

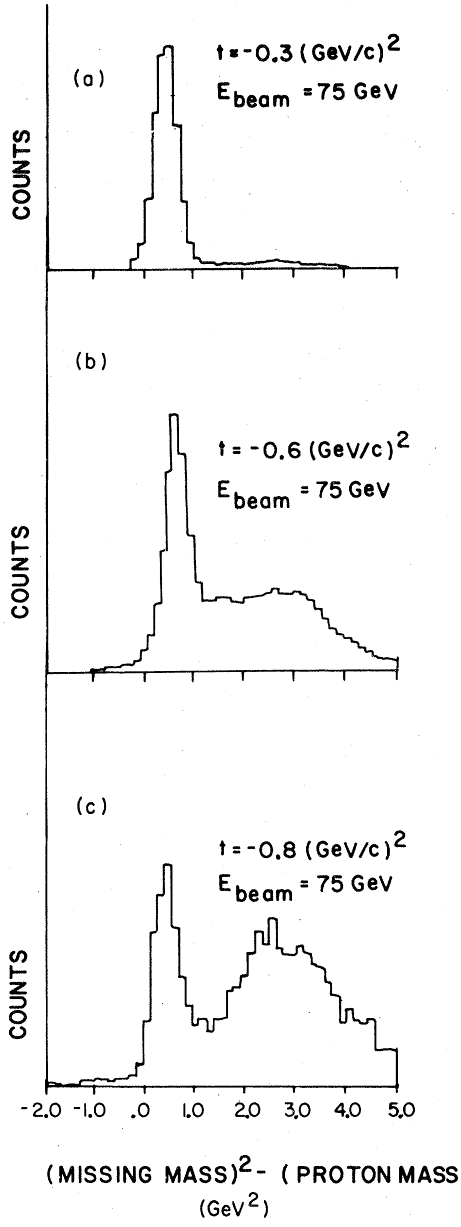

FIG. 11. (a) (Missing mass)^2 − (proton mass)^2 for $-t = 0.3$ (GeV/c)^2. (b) (Missing mass)^2 − (proton mass)^2 for $-t = 0.6$ (GeV/c)^2. (c) (Missing mass)^2 − (proton mass)^2 for $-t = 0.8$ (GeV/c)^2.

Since the data at some momenta were taken at different times, the time consistency of the data was checked. When this comparison was made, the asymmetries were found to be within statistical errors from one run to the next. The 0 and 180 degree runs were summed separately and their asymmetries calculated. The difference between the two orientations was less than one or two standard deviations for all points.

TABLE I. Elastic proton polarization.

t [(GeV/c)^2]	P_{beam} (GeV/c)	s (GeV^2)	P (polarization)
−0.3	20 ± 6	39.4	0.058 ± 0.015
	45 ± 8	86.3	0.011 ± 0.016
	77 ± 10	146.5	0.020 ± 0.013
	110 ± 10	208.6	0.003 ± 0.013
	176 ± 12	332.6	0.035 ± 0.014
	205 ± 15	387.2	0.026 ± 0.056
−0.6	22 ± 6	43.2	0.029 ± 0.014
	43 ± 10	82.6	−0.029 ± 0.017
	75 ± 12	142.8	−0.014 ± 0.015
	110 ± 10	208.6	−0.035 ± 0.017
	176 ± 12	332.6	−0.003 ± 0.018
−0.8	21 ± 6	41.3	0.038 ± 0.026
	45 ± 8	86.3	−0.042 ± 0.018
	76 ± 10	144.7	−0.036 ± 0.030
	110 ± 10	208.6	−0.014 ± 0.030
	176 ± 8	332.6	−0.021 ± 0.040
−1.0	22 ± 6	43.2	0.00 ± 0.057
	44 ± 8	84.5	0.123 ± 0.090
	75 ± 10	142.8	−0.075 ± 0.103
	110 ± 10	208.6	−0.144 ± 0.181

IV. DISCUSSION OF DATA

A. Elastic scattering

The measured asymmetries and calculated polarization for t values of -0.3, -0.6, -0.8, and -1.0 (GeV/c)^2 as a function of s are given in Table I. The data for all values of t covered a range of beam momenta from 20–175 GeV/c. The polarization for each of these t values as a function of s is shown in Table I; the errors shown are statistical.

At $t=-0.3$ (GeV/c)^2 (Fig. 12), the polarization falls from large positive values at low energies to near zero by $s \simeq 210$ GeV^2. However, at higher energies it appears that the polarization begins to rise again. More data would be needed for $s > 200$ GeV^2 to confirm this. Our result at $s = 40$ GeV^2 agrees well with results of Borghini *et al*;[3] there is also good agreement between our result and that of Gaidot *et al.*[4] at $s = 86$ GeV^2 and Fidecaro *et al.*[2] at $s = 282$ GeV^2.

At $t=-0.6$ (GeV/c)^2 (Fig. 13) and $t=-0.8$ (GeV/c)^2 (Fig. 14) the shape of the P versus s plot is very similar to that of $t=-0.3$ (GeV/c)^2. The polarization starts out large and positive at low energies and falls quickly with increasing energy. However, unlike the $t=-0.3$ (GeV/c)^2 result, between $s = 50$ GeV^2 and $s = 70$ GeV^2 the polarization becomes slightly negative and remains a few percent negative at least up to $s = 210$ GeV^2. This is confirmed by the Fidecaro *et al.*[2] data at $s = 282$ GeV^2. By $s = 330$ GeV^2 polarization appears to be rising again, but because of the statistical errors it is not clear if P remains a few percent negative or approaches zero. Again our results are in good agreement with other experimental results between $s = 43$ GeV^2 and $s = 83$ GeV^2.

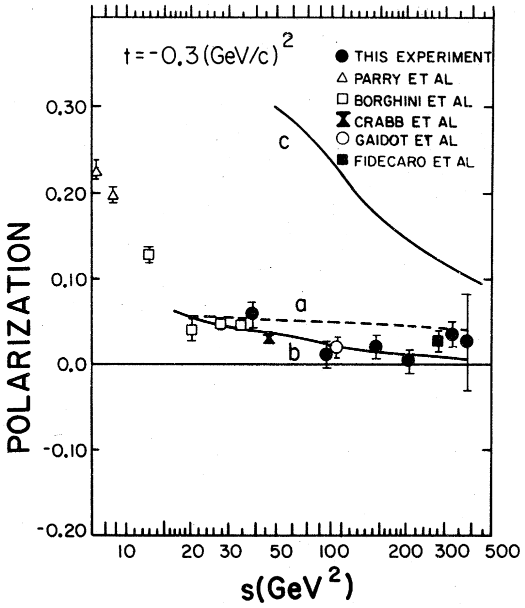

FIG. 12. Elastic proton polarization as a function of s for $-t=0.3$ (GeV/c)^2. Curve a, Pumplin and Kane (Ref. 16); curve b, Gerhold and Majerotto (Ref. 14); curve c, Wu, Bourrely, and Soffer (Ref. 17).

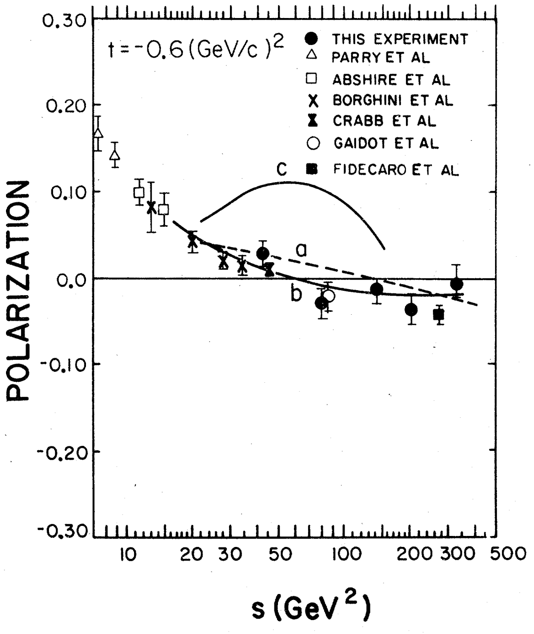

FIG. 13. Elastic proton polarization as a function of s for $-t=0.6$ (GeV/c)^2. Curve a, Pumplin and Kane (Ref. 16); curve b, Gerhold and Majerotto (Ref. 14); curve c, Wu, Bourrely, and Soffer (Ref. 17).

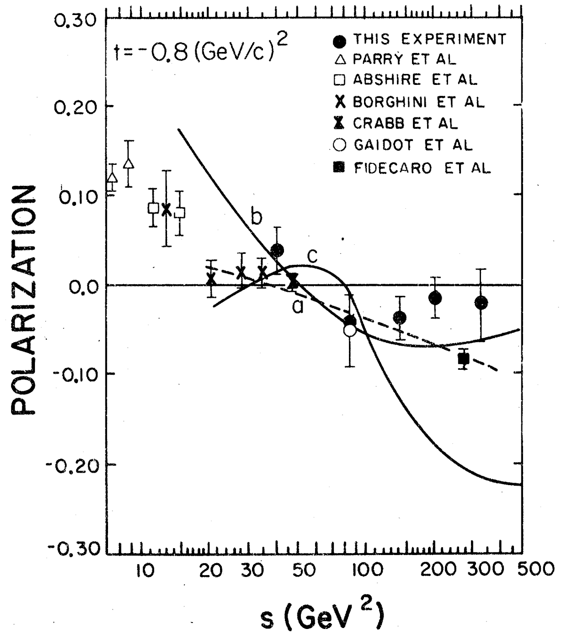

FIG. 14. Elastic proton polarization as a function of s for $-t = 0.8$ (GeV/c)^2. Curve a, Pumplin and Kane (Ref. 16); curve b, Gerhold and Majerotto (Ref. 14); curve c, Wu, Bourrely, and Soffer (Ref. 17).

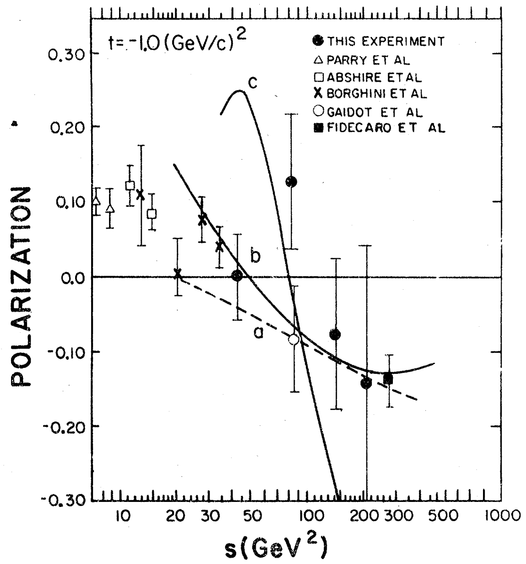

FIG. 15. Elastic proton polarization as a function of s for $-t = 1.0$ (GeV/c)^2. Curve a, Pumplin and Kane (Ref. 16); curve b, Gerhold and Majerotto (Ref. 14); curve c, Wu, Bourrely, and Soffer (Ref. 17).

At $t = -1.0$ (GeV/c)^2 (Fig. 15), the pattern at low energies is repeated: the polarization p is positive and fairly large at low energy and falls with increasing energy. The situation at $s = 86$ GeV^2, however, is not clear. There is some discrepancy between the result of this experiment, which is about +0.14 and the data of Gaidot *et al.*[4] which is about −0.08. The experimental error estimates for both points are large; however, more data would be needed to clear up the confusion. At both $s = 145$ GeV^2 and $s = 210$ GeV^2 the polarization was measured to be large and negative, about −0.15. Unfortunately, our error estimates are also large, but the data (especially that of Fidecaro *et al.*[2]) certainly indicate that the polarization is negative at these energies and may be quite large. We have no point at $s = 330$ GeV^2 for $t = -1.0$ GeV^2 because it was not possible to separate the elastic events from the inelastic background in this region.

B. Proton inclusive production

Table II contains the measured polarization for protons produced inclusively. The data are presented for each running configuration of transverse momentum (P_T) and Feynman x_F for both hydrogen and carbon targets. As was the case in elastic scattering, the polarization was cal-

TABLE II. Inclusive proton polarization.

						Polarization (×10^2)			
P (GeV/c)	θ (deg)	$\lvert x_F \rvert$	P_T (GeV/c)	Target	Analyzing power	$P_{\text{beam}} = 100$ GeV/c $s = 189.5$ GeV^2	200 GeV/c 377.0 GeV^2	300 GeV/c 564.7 GeV^2	400 GeV/c 752.3 GeV^2
0.56	64.11	0.9	0.5	H	0.189 ± 0.015	5.8 ± 2.0	8.4 ± 1.8	5.2 ± 1.8	0.3 ± 2.1
0.63	53.3	0.8	0.5	H	0.260 ± 0.015	6.4 ± 1.4	7.2 ± 1.4	6.9 ± 1.4	7.4 ± 1.5
0.73	43.6	0.7	0.5	H	0.289 ± 0.015	5.7 ± 1.8	7.9 ± 1.7	6.6 ± 1.8	7.0 ± 1.9
1.21	55.8	0.9	1.0	H	0.170 ± 0.030	2.4 ± 2.6	1.6 ± 2.2	0.0 ± 2.2	3.8 ± 2.2
1.21	55.8	0.9	1.0	C	0.170 ± 0.030	−7.1 ± 1.9	−7.1 ± 2.3	−6.7 ± 1.9	−9.8 ± 2.1
1.33	49.1	0.8	1.0	H	0.170 ± 0.030	−1.4 ± 1.6	2.4 ± 1.6	1.2 ± 1.6	−1.8 ± 1.7
1.43	42.6	0.7	1.0	H	0.170 ± 0.030	1.5 ± 1.9	2.1 ± 1.6	0.2 ± 1.6	1.3 ± 1.7
2.07	46.7	0.9	1.5	C	0.170 ± 0.030	−4.9 ± 2.9	−2.7 ± 2.6	−3.7 ± 2.6	2.6 ± 2.9
2.27	41.7	0.8	1.5	C	0.170 ± 0.030	−3.5 ± 2.9	2.7 ± 2.3	−0.5 ± 2.3	−0.1 ± 2.7

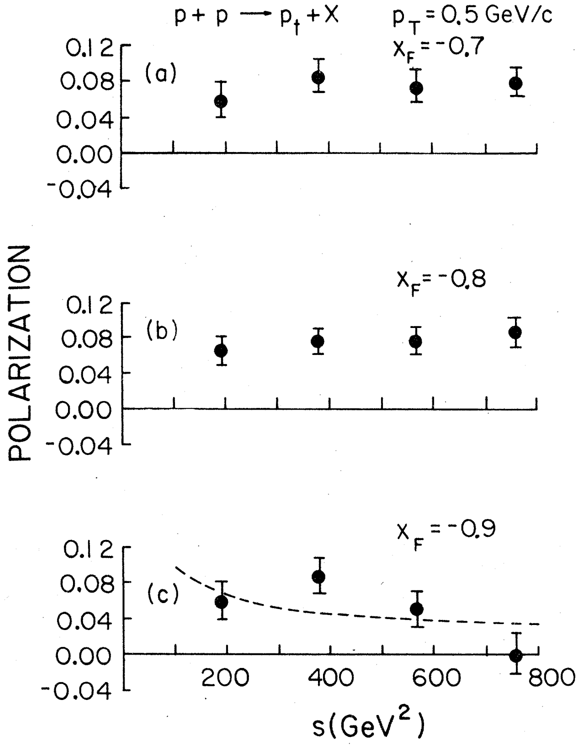

FIG. 16. Inclusive proton polarization as a function of s for $P_T = 0.5$ GeV/c, hydrogen target. (a) $x_F = -0.7$, (b) $x_F = -0.8$, (c) $x_F = -0.9$.

culated using the measured, energy-dependent carbon analyzing power listed in the table. The polarization data at each P_T and x_F value have been plotted as a function of beam energy in Figs. 16–18.

The data at $P_T = 0.5$ GeV/c in Fig. 16 show a distinct positive polarization for all values of beam energy. The data at $x_F = -0.7$ and -0.8 appear independent of beam energy. They have an average polarization value of +6%. At $x_F = -0.9$ there is an indication of a polarization decrease with beam energy. The general dependence is consistent with that expected from a triple-Regge model, as discussed in Sec. IV. This triple-Regge shape is indicated in Fig. 16.

At $P_T = 1.0$ GeV/c the hydrogen data is shown in Fig. 17. These data indicate no significant polarization for any measured beam energy or Feynman x_F. This is in marked contrast to the results obtained for Λ^0 inclusive production at the same energies and x_F values.[5]

The carbon target data at $P_T = 1.0$ GeV/c and $P_T = 1.5$ GeV/c are shown in Fig. 18. The $P_T = 1.0$ GeV/c data indicate a surprisingly large negative polarization, independent of beam energy. In view of the zero-polarization results from hydrogen we believe that this polarization is due to a low-energy secondary interaction in the carbon nucleus. This effect is discussed in Sec. V C. The $P_T = 1.5$ GeV/c data again indicate this negative-polarization effect which appears to be suppressed at higher recoil momentum.

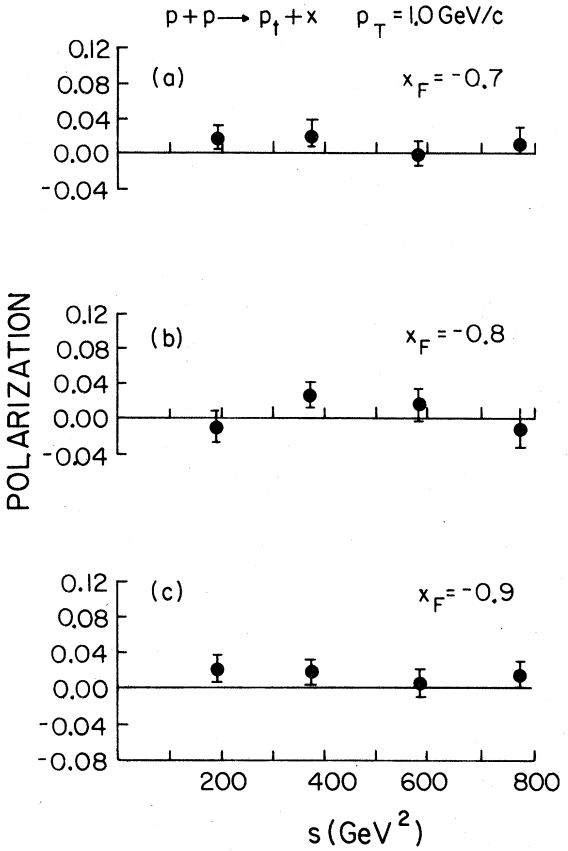

FIG. 17. Inclusive proton polarization as a function of s for $P_T = 1.0$ GeV/c, hydrogen target. (a) $x_F = -0.7$, (b) $x_F = -0.8$, (c) $x_F = -0.9$.

V. INTERPRETATION OF RESULTS

A. Elastic scattering

As is well known, the elastic scattering process for two spin-$\frac{1}{2}$ particles can be completely described by five amplitudes. A commonly used set[12,13] of five independent s-channel helicity amplitudes is

$$\phi_1 = \langle ++ | \phi | ++ \rangle, \quad \text{nonflip}$$

$$\phi_2 = \langle ++ | \phi | -- \rangle, \quad \text{double flip}$$

$$\phi_3 = \langle +- | \phi | +- \rangle, \quad \text{nonflip}$$

$$\phi_4 = \langle +- | \phi | -+ \rangle, \quad \text{double flip}$$

$$\phi_5 = \langle ++ | \phi | +- \rangle \quad \text{single flip}\,.$$

Other amplitudes can, of course, be chosen—for

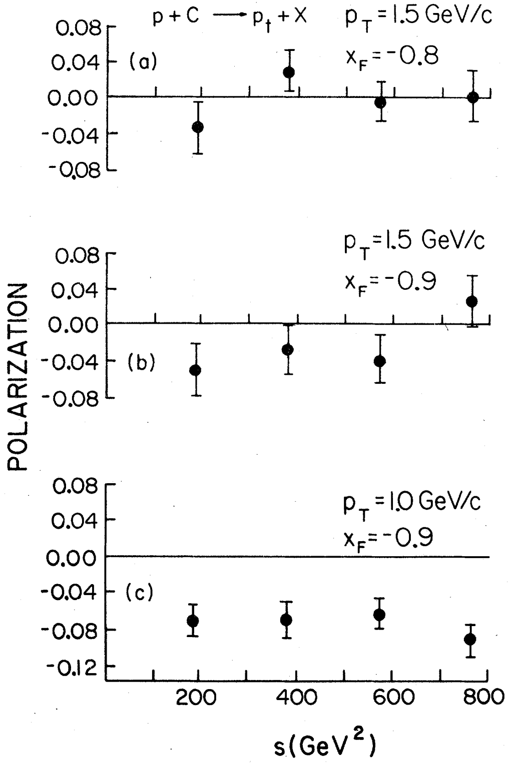

FIG. 18. Inclusive proton polarization as a function of s for $P_T = 1.0$ and 1.5 GeV/c, carbon target. (a) $x_F = -0.8$, (b) $x_F = -0.9$, (c) $x_F = -0.9$.

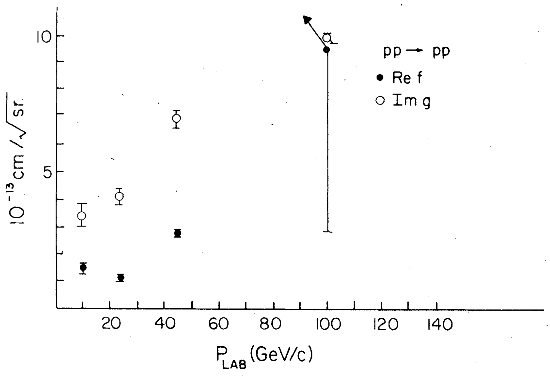

FIG. 19. Elastic amplitudes for proton-proton scattering from Hinotani *et al* (Ref. 13).

instance t-channel helicity amplitudes.

Any observable quantity such as the cross section (I_0), the polarization (P) or spin-correlation parameters can be easily expressed in terms of these amplitudes, such as

$$
\begin{aligned}
I_0 &= d\sigma/d\Omega\\
&= \tfrac{1}{2}(|\phi_1|^2 + |\phi_2|^2 + |\phi_3|^2 + |\phi_4|^2 + 4|\phi_5|^2)
\end{aligned}
$$

and

$$PI_0 = 2\,\mathrm{Im}[(\phi_5^*(\phi_1 + \phi_2 + \phi_3 - \phi_4)] .$$

Notice that the polarization is particularly sensitive to the value of the single flip amplitudes ϕ_5 while I_0 is not.

1. *Amplitude analysis*

One way to proceed in the investigation of the spin-dependent scattering amplitudes is to simply make enough measurements to determine uniquely all the amplitudes. At high energies there are as yet too few scattering measurements to yield a unique solution. However, several author (Gerhold and Majerotto[14] and Hinotani *et al.*[15]) have made model-dependent fits to this present data.

In a recent study Hinotani *et al.*[15] an attempt has been made to extract the behavior of the spin-flip amplitude from cross-section and polarization data. In this work it is assumed that at small t, pp elastic scattering can be suitably described by a spin-flip and nonflip amplitude and that, in this range, the nonflip amplitude dominates in magnitude and is orthogonal to the flip amplitude in phase. The results of this study show that the reduced spin-flip amplitude (i.e., the spin flip amplitude with the kinematic factor removed) is exponential in t. It is found that the slope of this functional dependence is comparable for pp and $\pi^{\pm}p$ elastic scattering. Furthermore, it is observed that the slope is practically independent of energy and that at $t = 0$ the reduced spin-flip amplitude is comparable to the spin-nonflip amplitude. It should be noted, however, that the observed polarization is dominated by kinematical terms which suppress these amplitudes. The reduced spin-flip amplitude f and the nonflip amplitude g are shown in Fig. 19.

Gerhold and Majerotto[14] use an eikonal model for the ϕ_1, ϕ_5 amplitudes, of the form

$$\phi_1(s,t) = is\int_0^\infty b\,db(1 - e^{i\chi_0(s,b)})J_0(b\sqrt{-t}) ,$$

$$\phi_5(s,t) = s\int_0^\infty b\,db\chi_1(s,b)\,e^{i\chi_0(s,b)}J_1(b\sqrt{-t}) ,$$

and assume both Pomeron and Reggeon contributions to χ_0 and χ_1. Data at beam energies of 24 and 150 GeV were fit to determine a total of five parameters. The resulting determination of the polarization is shown in Figs. 12–15 (curve b). The customary approximations $\phi_1 \approx \phi_3$, $\phi_2 \approx -\phi_4 \approx 0$ were made.

2. *Pumplin-Kane model*

In a recent paper by Pumplin and Kane[16] consequences were investigated of the Pomeron having quantum numbers different from the vacuum. In

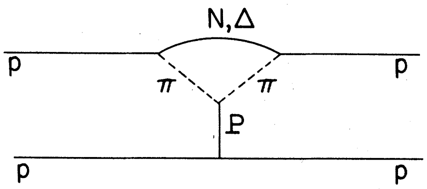

FIG. 20. Contribution to Pomeron exchange according to Pumplin and Kane (Ref. 16).

this paper they investigated the effects on nucleon-nucleon polarizations of the consequences of this assumption.

The possible contributions of graphs such as shown in Fig. 20 to both the flip (M_{+-}) and nonflip (M_{++}) amplitudes were evaluated. (Here the amplitude subscripts refer to the helicities of the upper vertex protons.) Estimates of the polarization were then obtained by fitting the ISR σ_{tot} and $d\sigma/dt$ data to the following formula:

$$M_{++} = is\,11.5 R^{2.21t} J_1(R\sqrt{-t})/\sqrt{-t} + is\,1.94 r^2 e^{3.93t} J_0(r\sqrt{-t}),$$

$$R^2 = 8.47 + 0.33(\ln s - i\pi/2),$$

$$r^2 = 2.92(\ln s - i\pi/2).$$

The first term in M_{++} is central in the impact parameter and the second term is peripheral in the impact parameter and is presumably due to the two-pion tail contribution. The contribution to the flip amplitude by the two-pion graph would then be expected to be of the form

$$M_{+-} = isC\,1.94 r^2 e^{3.93t} J_1(\sqrt{-t}),$$

where C is the flip/nonflip ratio calculated from the above graph. Knowledge of M_{++} and M_{+-} permits the calculation of the polarization. Predictions typical of those in their paper are illustrated in Figs. 12–15 as dashed curves (*a*).

It is of obvious interest that the full implications of this model and its ability to project the general features of high-energy polarizations be fully explored.

3. *Wu-Bourrely-Soffer model*

In a recent paper by Wu, Bourrely, and Soffer,[17] the effects of a rotating hadronic current distribution on the polarization in *p*-*p* elastic scattering has been investigated. The model is similar to the Chou-Yang model where the structure of the elastic *p*-*p* cross section over several orders of magnitude has been satisfactorily predicted. The rotating hadronic current can give rise to a finite spin-flip amplitude due to the differentiation between left and right available to an incoming proton. They have also assumed that the nonflip helicity amplitudes receive contributions only from the strong interaction and that the single-helicity flip amplitude arises purely from coulomb effects. In this way they were able to parametrize the polarization resulting from the interference between the coulomb amplitude and the hadronic amplitude. The predictions of this model with coulomb effects included, are shown in Figs. 12–15 (curve *c*). As can be seen from these figures it is possible to obtain a fair fit to the data with this model. The growth in magnitude of the polarization at large t is a feature of the model. Also, the trend at energies above 100 GeV for the polarization to go from positive at small t to large negative values at larger t is accounted for in the model.

B. Inclusive proton polarization with hydrogen target

1. *Amplitude analysis*

As was the case in elastic scattering, the polarization in an inclusive process can be related to a spin dependent (f) and spin independent (g) amplitude. This can be written as

$$P = -2\,\text{Im}[(f\sin\theta_{\text{c.m.}})^* g]/[|f\sin\theta_{\text{c.m.}}|^2 + |g|^2].$$

Since for spin-$\frac{1}{2}$–spin-0 scattering a multiplicative dependence on $\sin\theta_{\text{c.m.}}$ is found, we have chosen to explicitly display it in this expression.

The ratio of the spin-dependent to spin-independent amplitudes can, in general, be written

$$r' e^{i\phi} = f/g,$$

where r' is a real constant.

For all of our data points $\sin^2\theta_{\text{c.m.}}$ is less than 0.04. So, by neglecting terms that are second order in $\sin\theta_{\text{c.m.}}$ we obtain the expression

$$P = 2r'\sin\phi\sin\theta_{\text{c.m.}}.$$

The term $r = r'\sin\phi$ is the ratio of the orthogonal component of the spin-dependent amplitude to the orthogonal component of the spin-independent amplitude.

Using the relation above, r has been calculated for our data at $P_T = 1.0$ GeV/c and $P_T = 0.5$ GeV/c. The results are shown in Fig. 21 and Fig. 22. For $P_T = 1.0$ GeV/c, the ratio r is consistent with zero for all values of x_F and beam energy. In contrast, the ratio at $P_T = 0.5$ GeV/c is quite large and shows a distinct energy dependence. The value of r has a maximum of about 0.8 for a beam energy of 400 GeV. Although this is a crude calculation, the significance of spin-dependent amplitudes is readily apparent. It should be noted that the *observed* polarization is dominated by the kinematical factor $\sin\theta_{\text{c.m.}}$ in this forward region.

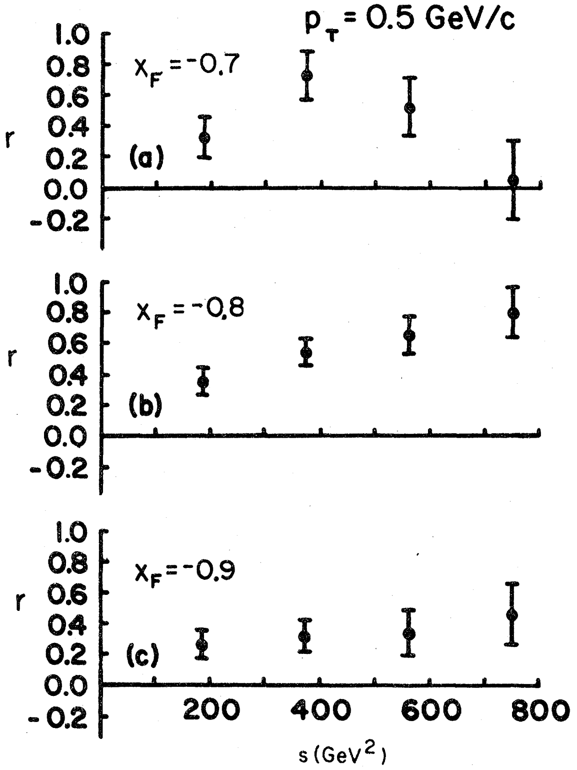

FIG. 21. r versus $E_{\rm lab}$ for $P_T = 0.5$ GeV/c. r is the ratio of spin-flip to nonflip orthogonal amplitudes. (a) $x_F = -0.7$, (b) $x_F = -0.8$, (c) $x_F = -0.9$.

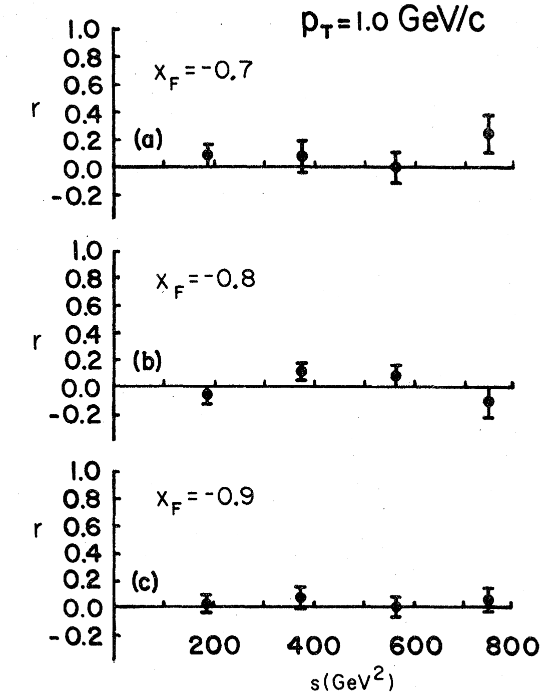

FIG. 22. r versus $E_{\rm lab}$ for $P_T = 1.0$ GeV/c. r is the ratio of spin-flip to nonflip orthogonal amplitudes. (a) $x_F = -0.7$, (b) $x_F = -0.8$, (c) $x_F = -0.9$.

2. *Triple-Regge models*

In the inclusive process predictions can be made for the cross section in the extreme forward direction when $|x_F| > 0.9$. This is the regime of the triple-Regge formalism. The polarization can be written[18]

$$P_c\sigma = (K/s)\sum_{ijk} P_{ijk}(s/M^2)^{\alpha_i(t)+\alpha_j(t)}(M^2)^{\alpha_K(0)},$$

σ is the invariant cross section for the process $p+p \to p+X$. K is a constant containing spin factors. The amplitude is shown in Fig. 23.

The triple-Regge couplings, P_{ijk}, have the property that nonzero polarizations occur only when the Reggeon $i \neq j$. Regge exchanges that are expected to give rise to polarization are *PRR* and *RRR*, where P represents a Pomeron and R a Reggeon exchange.

The model has been developed further by including more than three poles in the exchange and by adding the cut contributions to the equations.[19,20] These calculations do not differ from the model above in their predictions for the s dependence of the polarization.

Using the conventional Reggeon trajectories, $\alpha_P = 1 + \gamma t$ and $\alpha_R = 0.5 + \beta t$, we can rewrite the expression for the polarization as

$$P\sigma = Ks^{1/2}[P_{PRR}(1-x_F)^{-1-\beta t-\gamma t} + P_{RRR}(1-x_F)^{-0.5-2\beta t}].$$

In our experiment at each spectrometer setting x_F, P_T, and therefore t were held fixed and only s was allowed to vary. Since the invariant cross section in this kinematic region is dominated by the triple-Pomeron contribution it will scale as $(1-x_F)^{-1}$.[18] We would therefore expect that the polarization from the *PRR* and *RRR* exchanges

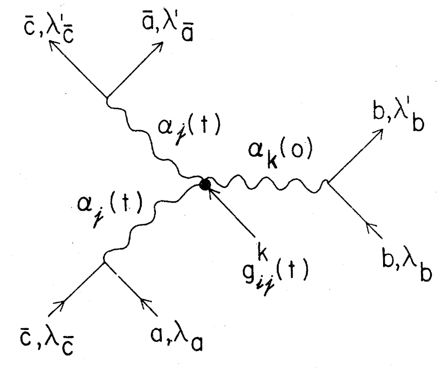

FIG. 23. Triple-Regge diagram for proton inclusive process.

would exhibit an $s^{-1/2}$ dependence at fixed x_F and t. A fit to the polarization data at $x_F = -0.9$, $p_T = 0.5$ GeV/c is shown in Fig. 16(c). At $P_T = 0.5$ GeV/c the data is best fit by $P = (0.9 \pm 0.2 \text{ GeV}/c)s^{-1/2}$. A similar fit to the $P_T = 1.0$ GeV/c, $x_F = -0.9$ data results in $P = (0.4 \pm 0.3 \text{ GeV}/c)s^{-1/2}$. As can be seen, the data do not show an energy dependence. However, the $s^{-1/2}$ dependence is not ruled out at the level indicated by the fit.

3. *Quark-model calculations*

There have been several attempts to relate spin phenomena to a constituent model of protons. To our knowledge all of these begin with a basic unexplained spin dependent quark-quark force. Using this elementary spin dependent amplitude, spin dependence of the composite systems are derived. In the case of elastic scattering at 90 degrees, Neal and Neilsen[21] have been able to analyze the 90 degree cross section and polarization data at high energy. Also, their model has been applied with some success to the new spin-correlation results.[15]

Anisovich and Shekhter[22] and others[23] have studied the application of the quark model to inclusive processes. In particular they have calculated polarization transfer properties for incident polarized protons for a wide variety of inclusive final states. However, these do not directly apply to our results without further model-dependent assumptions.

Heller[24] and Kane and Yao[25] have suggested a mechanism that would produce a predictable polarization in inclusive processes. In this picture a gluon creates a quark-antiquark pair which recombines with the incoming particle to form a specific inclusive channel, as in Fig. 24(a). If the spectator quark pair is in a relative s state, the resultant baryon has the same polarization direction as the original gluon. The analogy between QED photon bremsstrahlung polarization and quantum-chromodynamics gluon polarization suggests that there might be a net polarization determined only by the original gluon scattering direction. This picture appears to successfully explain the polarization as seen in Λ^0 production, and can be extended to proton inclusive processes as in Fig. 24(b). SU(6) calculations indicate that the proton polarization should be 60% of the Λ polarization.[24] Further refinements based on quark mass effects could reduce this to ~40%.[25] Of course either process shown in Fig. 24(b) represents a specific process to produce a given final state and certainly does not exclude other processes. However, one would conclude that if Fig. 24(b) did represent a substantial channel for proton inclusive production, then the proton polarization would, like the Λ case, increase with increasing P_T.[5] Since the observed proton polarization is very small and if anything decreasing with P_T, we must conclude that this mechanism is unimportant at these energies and P_T ranges.

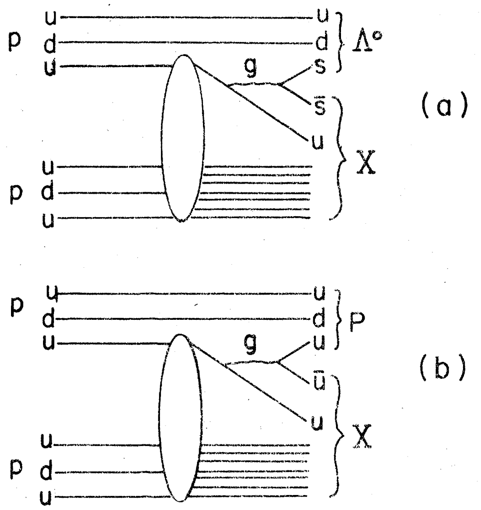

FIG. 24. (a) Gluon bremsstrahlung picture for inclusive polarization. (b) Gluon bremsstrahlung picture for proton inclusive polarization.

C. Polarization in $p + \text{C} \to p + X$

The indications of a very small polarization in p-p inclusive processes lead us to believe that the observed large polarizations from carbon must be due to nuclear effects. We have attempted to estimate the size of this possible effect with a very simply scattering model.

In this model we assume that there are only two basic interactions. First, the high energy beam proton interacts in the carbon nucleus and produces a distribution of particles. We assume that the resulting proton inclusive spectra are those measured for p-p interactions. Then we assume that one of the slow protons scatters while still in the carbon nucleus. This second interaction is assumed to be simple $p + \text{C} \to p_t + \text{C}$ scattering. We use the measured cross section and polarization for this process to calculate the proton polarization entering the spectrometer.

Since our measurement of the polarization of the recoil proton in $p + p \to p_t + X$ at a transverse momentum of 1.21 GeV/c was consistent with zero, the polarization of the first interaction was considered to be zero. The angular distribution of particles from the second interaction was assumed to be the differential cross section of $p + \text{C} \to p + X$ at an incoming beam momentum of 1.21 GeV/c (to match our measurements at $P_T = 1.0$ GeV/c). The scattered particles in $p + \text{C}$

$\rightarrow p_{\uparrow}+X$ are polarized. The polarization as a function of scattering angle is the analyzing power of carbon (A).

We used a fit to the proton inclusive spectra shown in Fig. 25(a). A fit to the differential cross section for $p+\mathrm{C}\rightarrow p+X$ as measured by Aebischer[26] is shown in Fig. 25(b). Data from Aebischer[26] and Eandi[27] was used for the carbon analyzing power. A plot of this analyzing power is shown as a function of the first interaction scattering angle in Fig. 25(c). The polarization was then calculated by combining and integrating these cross sections. The calculated polarization was found to be

$$P_{\mathrm{calc}}=-0.1\pm0.03,$$

which is in good agreement with our carbon data.

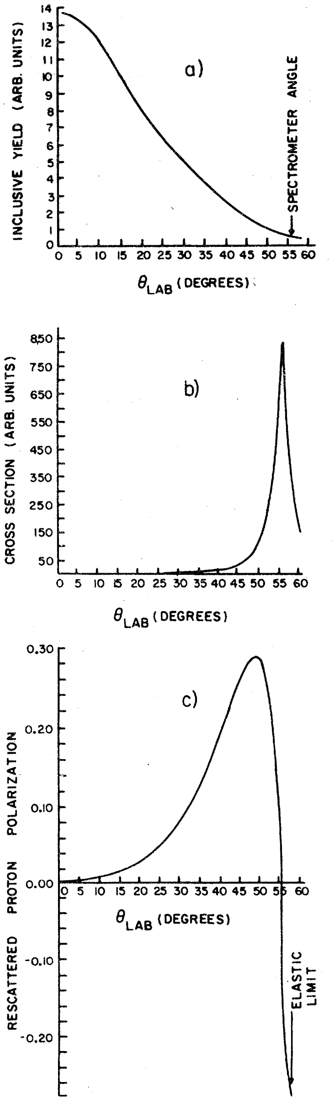

FIG. 25. (a) Inclusive proton spectrum at 400 GeV. (b) Proton-carbon scattering cross-sections at $P_{\mathrm{lab}}=1.21$ GeV/c. (c) Polarization of inclusive protons.

VI. SUMMARY

The polarization of the recoil proton in pp elastic scattering has been measured at beam momenta from 20 to 200 GeV/c. For all t values between -0.3 and -1.0 (GeV/c)^2 we observe a decrease of the polarization with increasing beam momentum. At low center-of-mass energies the polarizations are positive and agree well with existing measurements. However, at $t=-0.6$, -0.8, -1.0 (GeV/c)^2 the polarizations are negative for $s>100$ GeV^2. Large negative polarizations of -0.15% to -20% are seen at these t values. Several optical models have predicted this effect near the first minimum in pp scattering.

The polarization in the inclusive process $p+p\rightarrow p_{\uparrow}+X$ has been measured at $P_T=0.5$ GeV/c. The polarization appears independent of x_F, and s with an average value of 0.07 ± 0.02. However, at $P_T=1.0$ GeV/c this value drops to less than $2\%\pm2\%$. This observed decrease in the proton polarization with P_T is in contrast to that reported for the process $p+p\rightarrow\Lambda^0+X$. The energy independence is also not what one would predict from a triple-Regge model of inclusive polarization.

In the reaction $p+\mathrm{C}\rightarrow p_{\uparrow}+X$ we have measured a polarization of about -0.07 ± 0.02 at $P_T=1.0$ GeV/c, $x_F=-0.9$. We believe that this may be explained by a rescattering effect in the carbon nucleus.

ACKNOWLEDGMENTS

We wish to express our appreciation to all of those at the Fermi National Accelerator Laboratory who contributed to this experiment. In particular, we wish to thank the staff of the Fermilab Internal Target Area, led by Dr. T. Nash and Dr. P. McIntyre, for their assistance during set up and data taking. Also the cooperation of Argonne National Laboratory in the loan of a helium liquifiier contributed significantly to this experiment. We are indebted to several staff members and students for their assistance on this project, including P. Smith, B. Martin, M. Daskovsky, and F. Fredericksen, and to Prof. K. Hinotani and Wakayama Medical School, Wakayama, Japan. This work was supported by the U. S. Department of Energy.

APPENDIX: SIGN CONVENTION FOR THE POLARIZATION

The "Basel Convention" states that the positive polarization of particles with spin 1/2 is in the di-

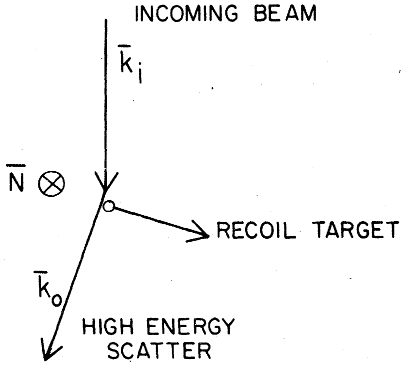

FIG. 26. Standard scattering convention for polarization direction.

rection $\vec{N}=\vec{k}_i\times\vec{k}_0$, where $\vec{k}_i$ and $\vec{k}_0$ are the momenta of the incoming and outgoing particles, respectively. This same convention holds in the center of mass system where $\vec{k}'_t=-\vec{k}'_b$ and $\vec{k}'_r\times\vec{k}'_s$. Here b, t, s, and r refer to beam, target, scattered, and recoil particles, respectively, and the primes indicate center of mass quantities. When identical particles are involved it is conventional to assume that the center of mass scattering angle is less than or equal to 90 degrees. In this experiment we always analyzed the slower particle in the laboratory frame which is the recoil particle. In Fig. 26 the beam is coming from the top and the scattered particle is going away from the spectrometer so that N, the direction of positive polarization is down.

The cross section for scattering in the carbon analyzer is

$$\sigma=\sigma_0(1+A\vec{P}\cdot\vec{M}),$$

where A is the analyzing power, $\vec{M}=(\vec{K}_i\times\vec{K}_0)/|\vec{K}_i\times\vec{K}_0|$, $\vec{P}$ is the polarization of the particles incident on the carbon, σ_0 is the unpolarized pC cross section, and $\vec{K}_i$ and $\vec{K}_0$ are the momenta of the incoming and outgoing particles. A has been measured to be positive in pC scattering at the energies and angles of this experiment. If P is pointing down as it is for positive proton polarization, the cross section will be larger for $\vec{M}$ pointing down and this is the case for a scatter to the right. Thus, a preponderance of scatters to the right indicates a positive polarization in the high-energy *pp* scattering.

For inclusive scattering we must preserve the convention in the limit $X\rightarrow 1$ or equivalently $M_X \rightarrow M_P$. Therefore the same conclusion is reached; that is, for positive polarization right scatters predominate.

---

*Present address: T. W. Bonner Nuclear Laboratory, Rice University, Houston, Texas 77001.

†Present address: LeCroy Research Systems Corp., 700 South Main Street, Spring Valley, NY 10977

‡Present address: Physics Dept., University of Maryland, College Park, MD 20747

§Present address: Argonne National Lab, Argonne, IL 60439

‖Present address: D908 Naval Avionics Center, 600 E. 21st, Indianapolis, IN 46218

[1] G. W. Abshire *et al.*, Phys. Rev. Lett. 32, 1261 (1974).

[2] G. Fidecaro *et al.*, Phys. Lett. 76B, 369 (1978).

[3] M. Borghini *et al.*, Phys. Lett. 31B, 405 (1970); 36B, 501 (1971).

[4] A. Gaidot *et al.*, Phys. Lett. 61B, 103 (1976).

[5] K. Heller *et al.*, Phys. Rev. Lett. 41, 607 (1978); G. Bunce *et al.*, Phys. Rev. Lett. 36, 1113 (1976).

[6] D. G. Crabb *et al.*, Phys. Rev. Lett. 41, 1257 (1978).

[7] S. Erhan *et al.*, University of California–Los Angeles Report No. UCLA-1122 (unpublished).

[8] M. Corcoran *et al.*, Phys. Rev. Lett. 40, 1113 (1978).

[9] R. Polvado *et al.*, Phys. Rev. Lett. 20, 20 (1979).

[10] P. Mantsch and F. Turkot, Fermilab Technical Memo No. TM-582, 1975 (unpublished); P. Mantsch and F. Turkot, Fermilab Technical Memo No. TM-586, 1975 (unpublished).

[11] G. W. Bryant *et al.*, Indiana University Internal Report No. C00-2009-102 (unpublished).

[12] H. Neal, in *High Energy Physics with Polarized Beams and Targets*, edited by M. L. Marshak (American Institute of Physics, New York, 1976), p. 3.

[13] M. L. Goldberger *et al.*, Phys. Rev. 120, 2250 (1960).

[14] H. Gerhold and W. Majerotto, Lett. Nuovo Cimento 23, 281 (1978).

[15] K. Hinotani *et al.*, Nuovo Cimento 52A, 363 (1979). (unpublished).

[16] J. Pumplin and G. L. Kane, Phys. Rev. D 11, 1183 (1975).

[17] T. T. Wu, C. Bourrely, and J. Soffer, Phys. Lett. 76B, 505 (1978). C. Bourrely, and J. Soffer, Lett. Nuovo Cimento 19, 569 (1977).

[18] R. Field and G. Fox, Nucl. Phys. B80, 367 (1974).

[19] F. E. Paige and D. P. Sidhu, Phys. Rev. D 13, 3015 (1976).

[20] G. R. Goldstein and J. F. Owens, Nucl. Phys. B103, 145 (1976).

[21] H. Neal and H. Nielsen, Phys. Lett. 51B, 79 (1974).

[22] V. V. Anisovich and V. M. Shekhter, Nucl. Phys. B55, 455 (1973).

[23] A. B. Zamolodchikov, B. Z. Kopeliovich, and L. I. Lapidus, Yad. Fiz. 26, 399 (1977) [Sov. J. Nucl. Phys. 26, 209 (1977)].

[24] K. Heller, University of Michigan Report No. UM HE 77-38 (unpublished).

[25] G. Kane and Y. Yao, University of Michigan Report No. UM HE 77-44 (unpublished).

[26] D. Aebischer, B. Favier, G. Greeniaus, R. Hess, A. Junod, C. Lechanoine, J. C. Nikles, D. Rapin, and D. Werren, Nucl. Instrum. Methods 124, 49 (1975).

[27] R. D. Eandi, R. W. Kenney, and V. Z. Peterson, Nucl. Instrum. Methods 32, 213 (1965).